Available online at www.sciencedirect.com
ScienceDirect
Trans. Nonferrous Met. Soc. China 35(2025) 1122−1136

Transactions of
Nonferrous Metals
Society of China
www.tnmsc.cn

Influence of microstructure uniformity on fracture behavior of magnesium alloy rolling sheet based on slip trace analysis

Jing TIAN[1,2,3,4], Jia-fei DENG[2,3,4], Wei LIANG[2,3,4], Xi ZHAO[1], Xiao-gang WANG[5]

1. School of Aerospace Engineering, North University of China, Taiyuan 030051, China;
2. Instrumental Analysis Center, Taiyuan University of Technology, Taiyuan 030024, China;
3. College of Materials Science and Engineering, Taiyuan University of Technology, Taiyuan 030024, China;
4. Shanxi Key Laboratory of Advanced Magnesium-based Materials, Taiyuan University of Technology, Taiyuan 030024, China;
5. Shanxi Yinguang Huasheng Magnesium Co., Ltd., Wenxi 043800, China

Received 20 May 2023; accepted 21 June 2024

Abstract: The nonuniform microstructure of magnesium alloy rolled sheets tends to influence their plastic deformation capacity. This study employed multi-pass restricted rolling to successfully prepare AZ31 magnesium alloy rolled sheets with a uniform microstructure, enhancing their mechanical properties. Quasi-in-situ tensile EBSD was used to investigate the effect of microstructure uniformity on the plastic deformation and fracture behavior of magnesium alloy. The results demonstrate that the nonuniformity of the magnesium alloy microstructure intensifies the strain asynchrony between adjacent grains, leading to relative misalignment and crack formation. Fine grains cannot coordinate the strain within their adjacent coarse grains, resulting in ledge formation at their common grain boundaries. Moreover, low-angle grain boundaries (LAGB) influence fracture behavior, rendering fine grains penetrated by LAGB more susceptible to becoming strain concentration areas that promote intergranular fracture and even transgranular fracture.

Key words: AZ31 magnesium alloy; rolling; microstructure; fracture behavior; plastic deformation

1 Introduction

As the lightest structural metal, deformed magnesium alloy sheets exhibit wide applicability in electronics, communication, transportation, and aerospace fields [1−4]. However, due to the low symmetry of magnesium crystal structure, the plastic deformation of magnesium alloy is not uniform [5−7]. Consequently, magnesium alloy sheets are prone to edge cracking during rolling, limiting single-rolling reduction and directly affecting material productivity and formability [8,9].

The microstructure of magnesium alloy rolled sheets often exhibits nonuniform grain size distribution. This nonuniformity exacerbates subsequent deformation [10], resulting in low plastic deformation capacity of magnesium alloy rolled sheets, affecting mechanical properties, and potentially leading to rapid material failure. Therefore, improving the microstructure uniformity of magnesium alloy rolled sheets can prevent premature fracture and effectively enhance plastic formability.

Microstructure nonuniformity of magnesium alloys is widely studied by scholars [9−12]. The microstructure nonuniformity of rolled magnesium alloy correlates closely with local area twinning, dynamic recrystallization (DRX), and shear band accumulation [6,13,14]. In our previous studies, we

---

Corresponding author: Xi ZHAO, Tel: +86-13934204597, E-mail: zhaoxi_1111@163.com
DOI: https://doi.org/10.1016/S1003-6326(24)66738-5

also found that both sparse shear bands and dense shear bands exist in rolled magnesium alloys, and during the subsequent annealing process, sparse shear bands develop into coarse grains, while dense shear bands develop into fine grains. At the same time, DRX is a heat-activation-related process that releases system energy when the stored energy in the crystal accumulates to a certain level during the thermal deformation process [15,16]. The occurrence of DRX and local grain size change are closely tied to crystal deformation storage energy and local strain state. Additionally, BARNETT et al [17] investigated the extrusion deformation of AZ31 and found that the transfer of twinning at the front end of the Lüders band intensifies the nonuniform changes of the microstructure. The obvious twinning interface between the twinned and untwinned regions hinders the subsequent deformation, so the deformed microstructure with activated twins tends to have significant nonuniformity [18−20]. However, there is still a lack of investigation on the tissue homogeneity of magnesium alloy rolled sheets, as follows:

(1) Few mechanisms have been reported for the effect of microstructure uniformity on the subsequent plastic deformation behavior of magnesium alloys.

(2) The investigation of the mechanism of the effect of tissue homogeneity on the fracture behavior of magnesium alloys is still very scarce.

Based on the above background, in this work, homogeneous magnesium alloy sheets were successfully prepared via multi-pass restricted rolling and an effective method to eliminate the inhomogeneous rolled microstructure was proposed. Quasi-in-situ analysis was used to trace the plastic deformation and fracture behavior of inhomogeneous and homogeneous magnesium alloy rolling states, respectively, investigating the influence of the homogeneity on the plastic deformation and fracture mechanism of magnesium alloy. This work provides theoretical supplements and technical guidance to improve the microstructure nonuniformity of magnesium alloy rolled sheets, improve the mechanical properties of magnesium alloy sheets, and expand industrial production applications.

2 Experimental

2.1 Material processing

In this work, the 3 mm-thick AZ31 magnesium alloy sheet was rolled by conventional rolling and multi-pass restricted rolling respectively. The restricted rolling process was explained in our previous research [8]. The rolling temperature was 400 °C and the rolling speed was 70 mm/s. By conventional rolling, magnesium alloy sheets with nonuniform microstructure under single reduction of 30% and 50% were prepared, respectively. The magnesium alloy sheet with uniform microstructure was prepared by two-pass restricted rolling, with a first reduction of 30% and a total reduction of 50%. The magnesium alloy sheet with uniform microstructure prepared by multi-pass restricted rolling was compared with the magnesium alloy sheet with nonuniform microstructure prepared by conventional rolling. To eliminate the residual stress, the two groups of magnesium alloys were annealed at 473 °C for 30 min.

2.2 Microstructure characterization

In the prepared magnesium alloy sheets, rectangular samples with dimensions of 8 mm (length) × 4 mm (width) were processed, corresponding to the rolling direction (RD) and transverse direction (TD). The microstructure of RD−ND (normal direction) surface of the samples was observed by optical microscope (OM; Leica–2500M). In addition, the microstructure of the RD−TD plane of samples with uniform and nonuniform microstructure was characterized by a high-resolution scanning electron microscope (SEM; S8000; TESCAN) equipped with electron backscattered diffraction (EBSD, Oxford), and representative areas were selected for quasi-in-situ tensile EBSD analysis.

The quasi-in-situ tensile samples were made into flat dog bone shapes by electronic discharge machining (EDM), and the sample size was 45 mm (length) × 6 mm (width) × 1 mm (thickness). The tensile test was performed at room temperature with a constant displacement rate of 1 μm/s. To ensure that the tensile table clamps the tensile samples firmly, a preload of 20 N was applied before loading. Tensile samples were paused at different strain stages for EBSD measurements and secondary electron (SE) SEM high-resolution imaging.

The surfaces of EBSD samples were prepared by mechanical grinding with SiC sandpaper of different roughness in turn. The electrochemical polishing was performed in the electrolyte with 5% perchloric acid and 95% ethanol at 0.35 A and 45 V for 60 s, and the electrolysis temperature was between −20 and −30 °C. After electropolishing, the surface of the sample is bright without deep pits. Finally, the obtained EBSD data were processed using Channel 5 software.

2.3 Plastic deformation analysis

Based on SEM images and EBSD data acquired during the test, slip trace analysis was performed to identify activated slip systems. Five slip modes with 30 slip systems usually encountered in magnesium alloys [10,21−26] are considered, as given in Table 1.

Combined with the slip traces observed inside specific grains in the SEM images and the average grain orientation of a specific grain obtained from EBSD, a self-made MATLAB code was used to calculate all possible slip plane traces and corresponding Schmid factors (SFs) of the corresponding slip system. Based on the best match of the observed slip trace with the calculated results, a specific slip system was selected as the activated slip system.

Figure 1 shows an illustration of slip trace analysis within G55 at a strain of 10% for the magnesium alloy studied. The horizontal direction in Fig. 1 indicates the quasi-in-situ tensile loading direction, and the horizontal directions in all SEM images and EBSD images in this work indicate the loading direction. In the SEM image of G55 (Fig. 1(b)), the slip trace parallel to the red dashed line in grain consists of actual slip traces of G55. According to the IPF map shown in Fig. 1(a), the three Euler angles of Grain 55 are 34.54°, 19.27°, and 35.21°, respectively. The theoretical slip trace calculated by the three Euler angles is shown in Fig. 1(c). The solid red line matches the actual slip trace well, indicating that basal ⟨*a*⟩ slip is activated in G55. The small deviation between the calculated results and the actual slip trace may be due to lattice distortion caused by deformation.

Combining the SFs of the different variants of the basal ⟨*a*⟩ slip system in Table 1, we determine that basal slip $(0001)[\bar{1}2\bar{1}0]$ with the highest SF value was activated in G55. Notably, the method cannot be used for determination when the Burgers vector of slip is parallel to the observation plane or dislocations do not move to the sample surface. Nevertheless, slip trace analysis is still an effective means to quantitatively study a large number of grain deformation modes [27−29].

Table 1 Schmid factors of different slip systems of G55

Slip mode	No.	Slip system	Schmid factor
Basal ⟨*a*⟩ slip	1	$(0001)[2\bar{1}\bar{1}0]$	0.14
	2	$(0001)[\bar{1}2\bar{1}0]$	0.17
	3	$(0001)[\bar{1}\bar{1}20]$	0.03
Prismatic ⟨*a*⟩ slip	4	$(01\bar{1}0)[2\bar{1}\bar{1}0]$	0.47
	5	$(10\bar{1}0)[\bar{1}2\bar{1}0]$	0.33
	6	$(\bar{1}100)[\bar{1}\bar{1}20]$	0.14
Pyramidal I ⟨*a*⟩ slip	7	$(01\bar{1}1)[2\bar{1}\bar{1}0]$	0.35
	8	$(\bar{1}011)[\bar{1}2\bar{1}0]$	0.21
	9	$(1\bar{1}01)[\bar{1}\bar{1}20]$	0.13
	10	$(10\bar{1}1)[\bar{1}2\bar{1}0]$	0.37
	11	$(\bar{1}101)[\bar{1}\bar{1}20]$	0.11
	12	$(0\bar{1}11)[2\bar{1}\bar{1}0]$	0.48
Pyramidal I ⟨*c*+*a*⟩ slip	7-1	$(01\bar{1}1)[\bar{1}2\bar{1}\bar{3}]$	0.29
	8-1	$(\bar{1}011)[\bar{1}\bar{1}2\bar{3}]$	0.02
	9-1	$(1\bar{1}01)[2\bar{1}\bar{1}\bar{3}]$	0.23
	10-1	$(10\bar{1}1)[2\bar{1}\bar{1}\bar{3}]$	0.10
	11-1	$(\bar{1}101)[\bar{1}2\bar{1}\bar{3}]$	0.49
	12-1	$(0\bar{1}11)[\bar{1}\bar{1}2\bar{3}]$	0.05
	7-2	$(01\bar{1}1)[11\bar{2}\bar{3}]$	0.10
	8-2	$(\bar{1}011)[\bar{2}11\bar{3}]$	0.13
	9-2	$(1\bar{1}01)[1\bar{2}1\bar{3}]$	0.30
	10-2	$(10\bar{1}1)[11\bar{2}\bar{3}]$	0.10
	11-2	$(\bar{1}101)[\bar{2}11\bar{3}]$	0.43
	12-2	$(0\bar{1}11)[1\bar{2}1\bar{3}]$	0.20
Pyramidal II ⟨*c*+*a*⟩ slip	13	$(2\bar{1}\bar{1}2)[2\bar{1}\bar{1}\bar{3}]$	0.19
	14	$(11\bar{2}2)[11\bar{2}\bar{3}]$	0.01
	15	$(\bar{1}2\bar{1}2)[\bar{1}2\bar{1}\bar{3}]$	0.43
	16	$(\bar{2}112)[\bar{2}11\bar{3}]$	0.32
	17	$(\bar{1}\bar{1}22)[\bar{1}\bar{1}2\bar{3}]$	0.02
	18	$(1\bar{2}12)[1\bar{2}1\bar{3}]$	0.28

In addition, in special cases, we use the Lustre−Morris parameter (geometric compatibility factor) to express the degree of strain compatibility between activated slip systems in adjacent grains. This parameter describes the correlation between the adjacent slip plane normal and slip directions,

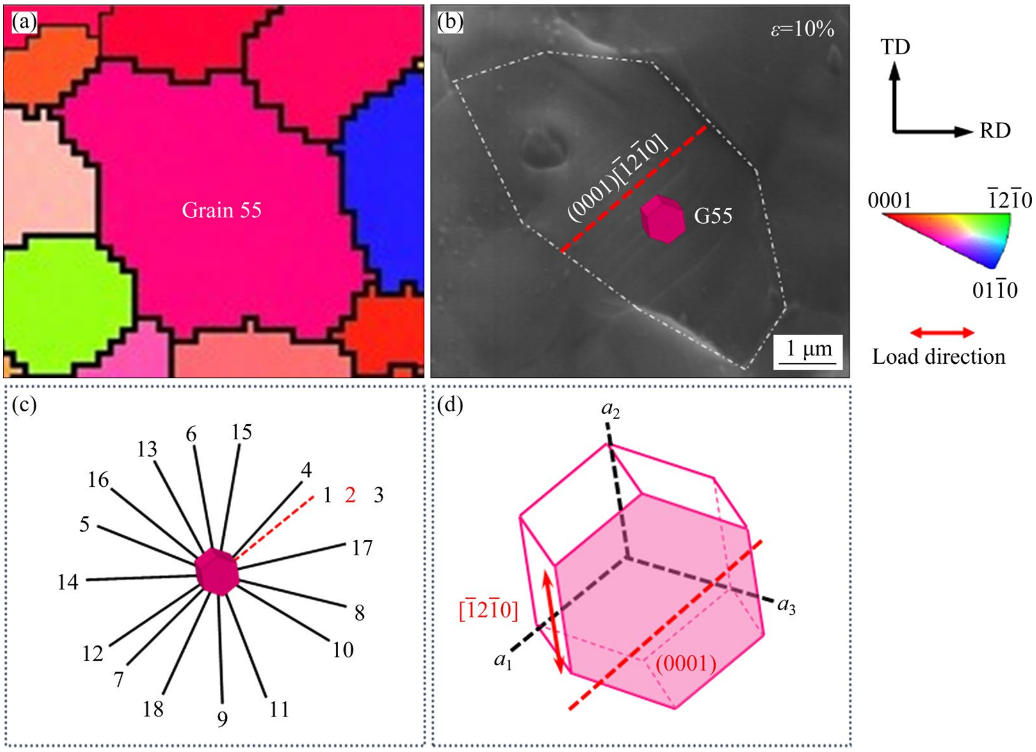

Fig. 1 Slip trace analysis: (a) IPF map; (b) SEM image; (c) Potential slip traces; (d) Unit cell of G55

defined as follows [23,30]:

$$m'=\cos\kappa\cdot\cos\psi \tag{1}$$

where the angles κ and ψ respectively denote the angle between the slip direction of the two slip systems involved and the normal of the slip planes. m' is in the range [0,1] and the closer it is to 1, the more geometrically compatible the two systems are.

3 Results

3.1 Homogenized microstructure by multi-pass restricted rolling

Figure 2 shows the morphologies of the AZ31 magnesium alloy sheet after different passes of restricted rolling and annealing. After one pass of rolling, the rolling microstructure of the magnesium alloy is not uniformly distributed, and corrugated shear bands are formed at the same time. After further two passes of rolling, the grain refinement is obvious, the recrystallization increases and the uniformity of the rolled sheet is improved significantly. After annealing, the equiaxed grains are formed in magnesium alloy sheet with uniform coarseness and fineness, showing uniformly distributed grain, as shown in Fig. 2(c). Multi-pass restricted rolling can effectively improve the uniformity of the microstructure distribution of the magnesium alloy.

In addition, the microstructure of magnesium alloy sheets after different rolling processes is further compared, as shown in Fig. 3. The nonuniform microstructure of conventional rolling is in sharp contrast to the uniform microstructure after multi-pass restricted rolling.

3.2 Effect of microstructure uniformity on plastic deformation of magnesium alloy

To further study the influence of nonuniform microstructure and uniform microstructure on the plastic deformation of magnesium alloy, quasi-in-situ tensile tests were carried out, as shown in Fig. 4. Figure 4(c) shows the quasi-in-situ load−displacement curves of Mg alloy samples with nonuniform microstructure and uniform microstructure. The results show that the uniform microstructure and nonuniform microstructure have similar ultimate tensile strength (UTS), and the UTS of uniform microstructure is slightly higher, which is due to the grain refinement strengthening effect. It is noteworthy that uniform microstructure has a longer tensile plateau period compared to the nonuniform microstructure, and the nonuniform microstructure undergoes early fracture during the tensile process compared to the uniform microstructure. This shows that the microstructure

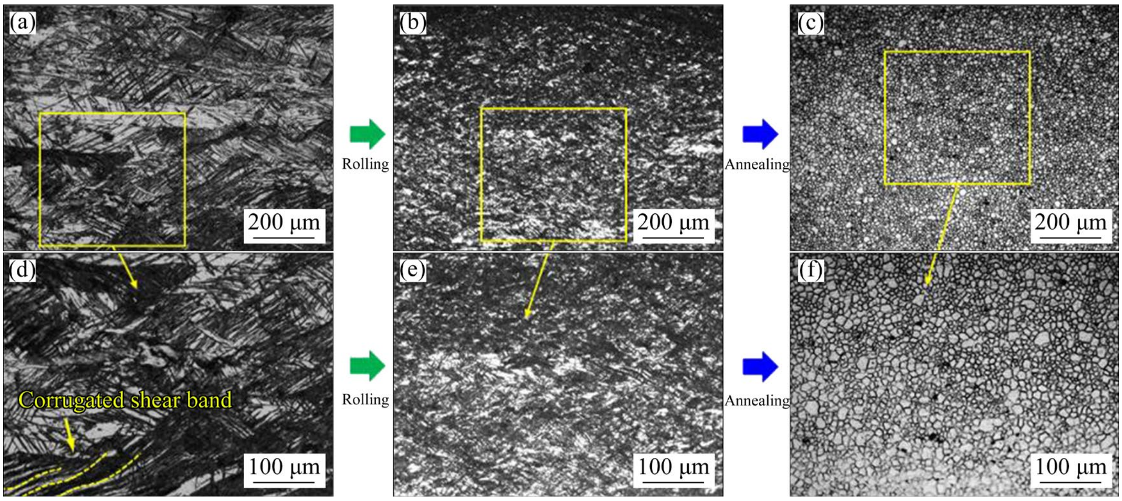

Fig. 2 Morphologies of AZ31 alloy sheet after restricted rolling and annealing: (a, d) After one pass; (b, e) After two passes; (c, f) Annealed microstructures after two-pass restricted rolling

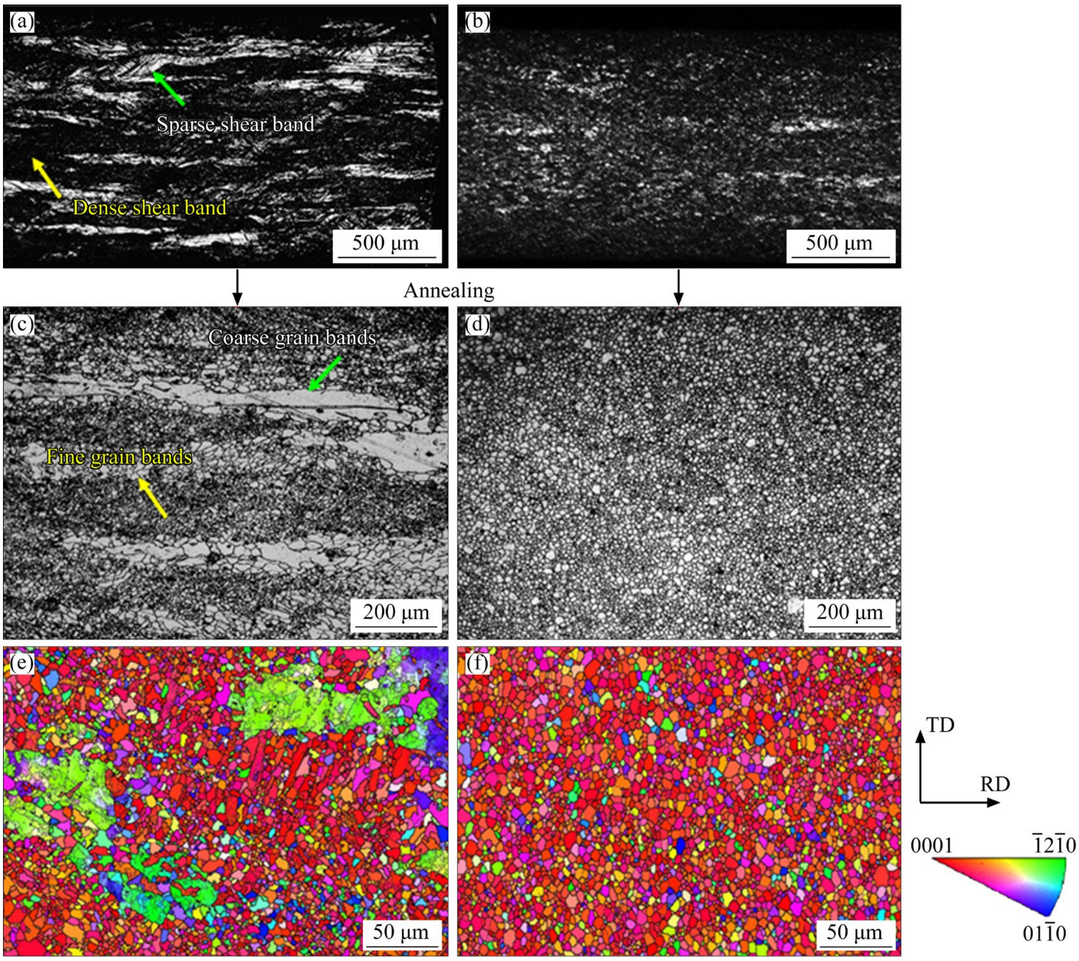

Fig. 3 Microstructures of AZ31 alloy rolled sheets: (a, c, e) Conventional rolling; (b, d, f) Multi-pass restricted rolling

uniformity affects both the plastic deformation behavior and the fracture behavior of the magnesium alloy.

The EBSD data and SE-SEM images were collected for the uniform microstructure sample at strains up to 8%, 10%, and 20%, and for the nonuniform microstructure samples at strains up to 10%, 11%, and 16%, respectively. Figures 4(a, b) correspond to the respective initial state microstructures, respectively, and Fig. 4(d) shows an IPF map of nonuniform microstructure at different strain stages. With increasing strain, the low-angle grain boundaries (LAGBs) within the coarse grains gradually increase, and the lattice distortion in the region adjacent to the coarse and fine grains increases, resulting in some grains being unrecognized (shown in black in Fig. 4(d)). Figure 4(e) shows the IPF image of the uniform microstructure at different strain stages. With the increase of strain, the number of grains with lattice distortion increases and the distribution becomes relatively uniform.

Figure 5 shows the SE-SEM images of nonuniform and uniform microstructures in different strain stages. It can be seen from Figs. 5(a−d) that as the strain increases, the fine grain area of the nonuniform microstructure initially forms a bumpy surface (shown by yellow solid circles in Fig. 5(b)), indicating that stress concentration occurs here first. As the load continues to increase, the slip increases, and the bumpy areas are distributed more in the area adjacent to the coarse and fine grains (around the white dashed line). When strained to fracture (ε=16%), these bumpy areas develop into

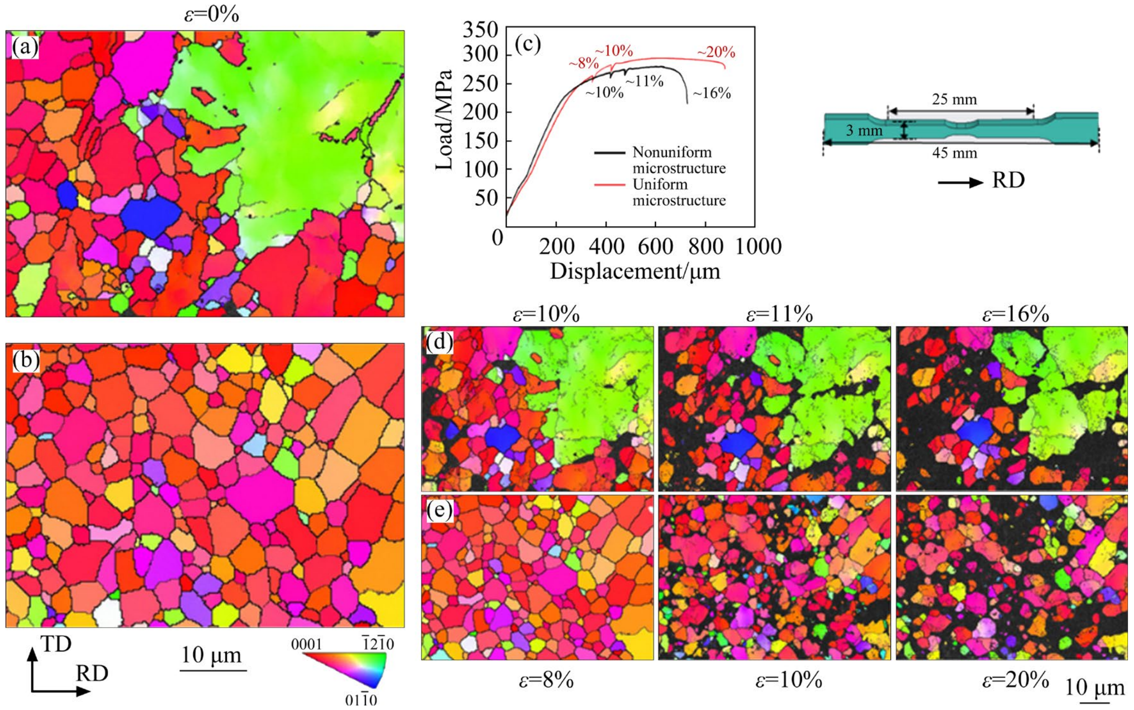

Fig. 4 Quasi-in-situ tensile results: (a, d) Nonuniform microstructures; (b, e) Uniform microstructures; (c) Load−displacement curves

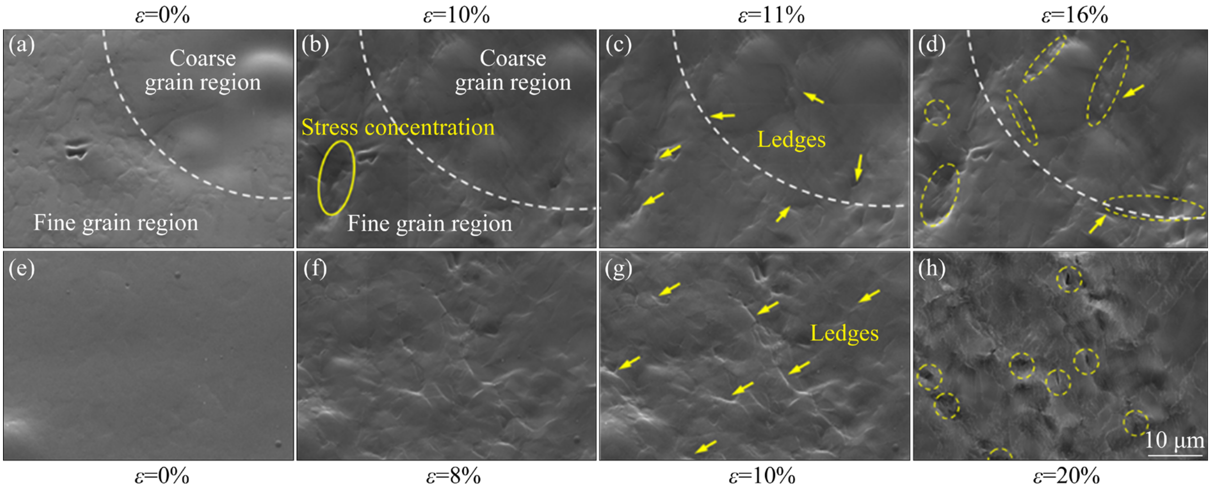

Fig. 5 SE-SEM images: (a−d) Nonuniform microstructures; (e−h) Uniform microstructures

microcracks (yellow dashed circles) or ledges (yellow arrows). Figures 5(e−h) show that the formation of bumpy areas is more random and dispersed during the stretching of a uniform microstructure, and the distribution of microcracks and ledges is more uniform when stretching to fracture.

The nonuniform microstructure is more likely to form strain concentrations and develop into cracks during deformation in the region adjacent to the coarse and fine grains, i.e., the region with the greatest microstructure differences, and therefore fracture earlier. In contrast, the formation of cracks is more random and uniform during deformation in uniform microstructure, ensuring better plastic deformation behavior and a longer plastic plateau period for samples with uniform microstructure.

4 Discussion

It is found that the plastic deformation behavior and fracture mechanism of AZ31 Mg alloy can be summarized into the following three situations: Grain-to-grain relative misalignment due to nonuniform deformation, strain coordination between coarse and fine grains, and fracture behavior affected by LAGB.

4.1 Grain-to-grain relative misalignment due to nonuniform deformation

Figure 6 shows two types of microcracks. As shown in Figs. 6(a−c), Crack-1 is formed at the common grain boundary between adjacent grains (G29 and G42).

Figure 6(a) shows the original microstructure, where basal slip is preferentially activated within G42 as strain increases, and the grain boundary between G29 and G42 forms a ledge. Meanwhile, basal slip $(0001)[\bar{1}\bar{1}20]$ is also activated in the adjacent G29, and the corresponding SF is 0.43. The ledge between G29 and G42 is more obvious. The strain coordination factor (m') between G29−G42 internal slip systems is calculated to be 0.25, which indicates that the strain between adjacent grains is not coordinated, and the local strain concentration leads to the formation of the ledge at the common grain boundary. Eventually, when stretched to the fracture stage (ε=16%), no new slip system is activated to accommodate the nonuniform strain between adjacent grains, and the ledge is converted to intergranular microcracks.

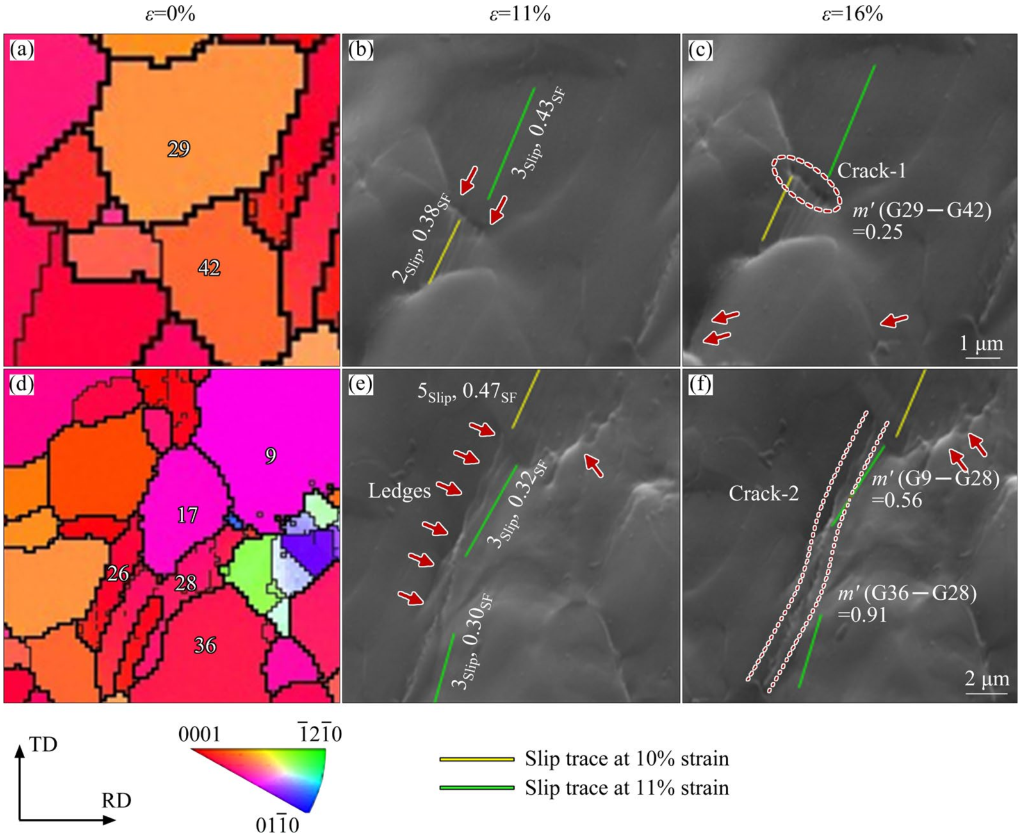

Fig. 6 Crack evolution in nonuniform microstructure: (a, d) IPF maps; (b, c, e, f) SEM images

The difference is that Crack-2 is formed at the common grain boundary of multi-grains (G17, G26, and G9, G28). Figure 6(d) shows the microstructure before stretching. When loading to 10% strain, the prismatic slip system $(10\bar{1}0)[\bar{1}2\bar{1}0]$ is activated in G9. With the increase of strain, slip systems are activated in G28 and G36, which are identified as basal slip $(0001)[\bar{1}\bar{1}20]$ by the slip trace method, and the corresponding SF values are 0.32 and 0.30, respectively. However, no-slip system is activated in G17 and G26. The ledge between G28 and G26 deepens and lengthens along the common grain boundary, and is connected with the ledge formed between G17 and G9. According to the calculation, the m' values between the pair of grains G9−G28 and G28−G36 are 0.56 and 0.91, respectively. This shows that among these three grains, the slip systems between adjacent grains are strain compatible, and dislocations more easily transfer between the two pairs of grains. In contrast, there is no significant slip trace between G17 and G26, indicating that the dislocations cannot be transferred between these grains or the dislocation movement is blocked. Under the same macro-strain condition, the dislocation movement on both sides of the local area is asynchronous, and the coordinated strain capacity varies widely, resulting in nonuniform deformation.

The side with well slip transmission (the area composed of G9, G28, and G36) is prone to strain concentration and the surface is full of bumps to form a kink, in contrast to the relatively smooth surface on the other side (the area composed of G17 and G26) (Fig. 6(f)). When stretched to fracture, these multigrain ledges transform into multigrain microcracks.

A similar situation is found for multi-grain intergranular cracks in uniform microstructures, as shown in Fig. 7. Crack-A, Crack-B, and Crack-C are formed on the common grain boundary of grain pairs G35−G28, G13−G14, and G40−G52, respectively (Fig. 7(c)), and Fig. 7(a) shows the microstructure at the initial stage. With the increase in load, there are slip traces in the grains on the right side of the observation area. According to trace analysis and identification, prismatic slip $(\bar{1}100)[\bar{1}\bar{1}20]$ is activated in G14, and second-order pyramidal slip $(\bar{1}\bar{1}22)[\bar{1}\bar{1}2\bar{3}]$ is activated in G17. The m' value between G14 and G17 internal slip systems is calculated as high as 0.83. At the same time, the basal slip $(0001)[\bar{1}2\bar{1}0]$ is activated in G29, the first-order pyramidal slip $(1\bar{1}01)[2\bar{1}\bar{1}\bar{3}]$ is activated in G39 and the second-order pyramidal slip $(2\bar{1}\bar{1}2)[2\bar{1}\bar{1}\bar{3}]$ is activated in G40. The m' value between the slip systems in the grain pairs G29−G40 and G39−G40 all is calculated as 0.90. The high value of the strain coordination factor indicates that the strain between grains on the right side of the observation area is compatible, and the movement of dislocations is not easily hindered. In

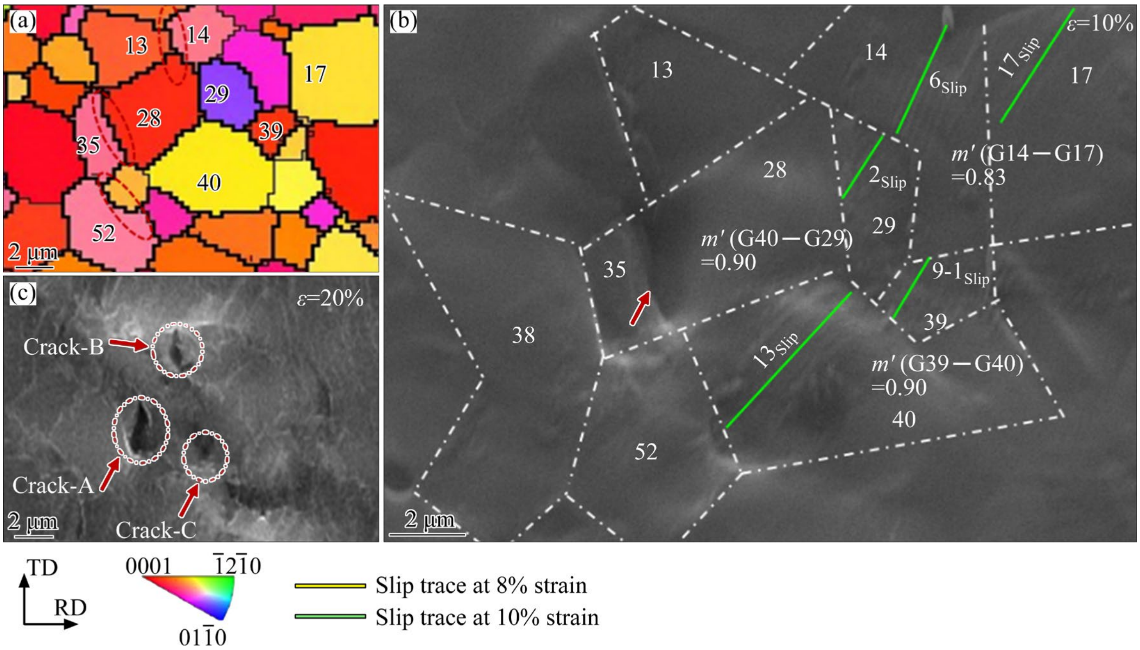

Fig. 7 Crack evolution in uniform microstructure: (a) IPF map; (b, c) SEM images

contrast, no obvious slip traces are generated in the left side of the observed region within the grains to carry the dislocation movement, and the dislocation movement is asynchronous on the left and right sides. The local strain is concentrated on the side with better dislocation movement, and the bumpy kink band is observed under SEM. Under the same macroscopic load, a shear crack is formed between the grain pairs with the largest relative strain, and the direction of crack generation is perpendicular to the load direction.

The mechanism of strain asynchrony and fracture caused by deformation nonuniformity is shown in Fig. 8. The blue line in the figure represents the slip trace and the larger the blue area is, the denser the slip trace is in the grain, and the more active slip system is. At the initial stage of deformation (Stage I), the slip system is preferentially activated in grain pair A−B, the strain of the deformation system between adjacent grains is compatible, and the dislocation movement is not hindered. On the other side of the grain pair, no slip occurs in C−D, because the dislocation movement is blocked, and the deformation at A−B cannot be transferred to C−D. In the later stage of deformation (Stage II), more slip systems are activated in the grain pair A−B to coordinate the deformation, and the strain increases. The strain of the left and right grain pairs is asynchronous, and the misalignment occurs, forming a ledge at the common grain boundary. Finally, as relative strain (misalignment) of the two-grain pairs increases, the ledge further expands into microcracks.

4.2 Strain coordination between coarse and fine grains

Figure 9 illustrates the fracture behavior between coarse and fine grains within the heterogeneous microstructure. From Fig. 9(c), Crack-1, and Crack-2 manifest at the shared grain boundary interface delineating coarse grains (G13) from fine grains (G91, G71). Upon reaching a strain of 10%, the common grain boundary of the grain pairs G13−G91 and G13−G71 bulges, forming ledges. Slip traces become apparent within G13, G91, and G70. The trace analysis identifies that prismatic slip $(10\bar{1}0)[\bar{1}2\bar{1}0]$ is activated in G13, first-order pyramidal $(1\bar{1}01)[\bar{1}\bar{1}20]$ slip is activated in G91, and second-order pyramidal slip $(\bar{1}2\bar{1}2)[\bar{1}2\bar{1}\bar{3}]$ is activated in G70. During the stretching leading to fracture, prismatic slip $(01\bar{1}0)[2\bar{1}\bar{1}0]$ becomes activated in G71.

There is no difference in the activated slip system type between coarse grain G13 and fine grains G71, G70, and G91. Therefore, the activated slip system type of coarse grains and fine grains is related to grain orientation rather than grain size.

Grain pairs, G13−G70, G13−G91, and G13−G71 have low m' values for intergranular slip transfer. Consequently, the transference of strain across coarse and fine grains poses a challenge. Moreover, the strain generated by the coarse grain G13 surpasses that generated within the fine grain, and the fine grain is not enough to coordinate the deformation generated by the coarse grain, further exacerbating the strain incompatibility between the coarse and fine grains, and fostering localized strain concentration. Ultimately, this localized strain concentration precipitates the development of protrusions and, in severe instances, initiates crack propagation along the shared grain boundary.

Similarly, the sample possessing a uniform microstructure also comprises coarse and fine grains, albeit with minimal disparity in grain size and a random distribution. Nonetheless, in the later stage of plastic deformation, this configuration remains susceptible to the initiation of microcracks, as illustrated in Fig. 10. Figure 10(a) depicts the

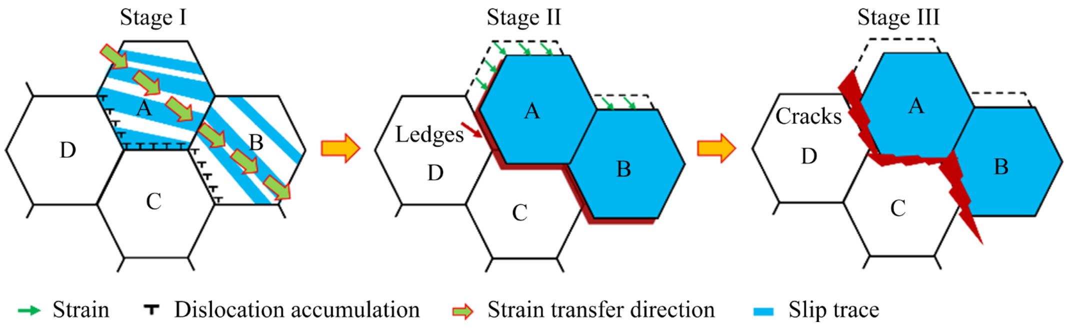

Fig. 8 Mechanism diagram of strain asynchrony and fracture caused by deformation nonuniformity

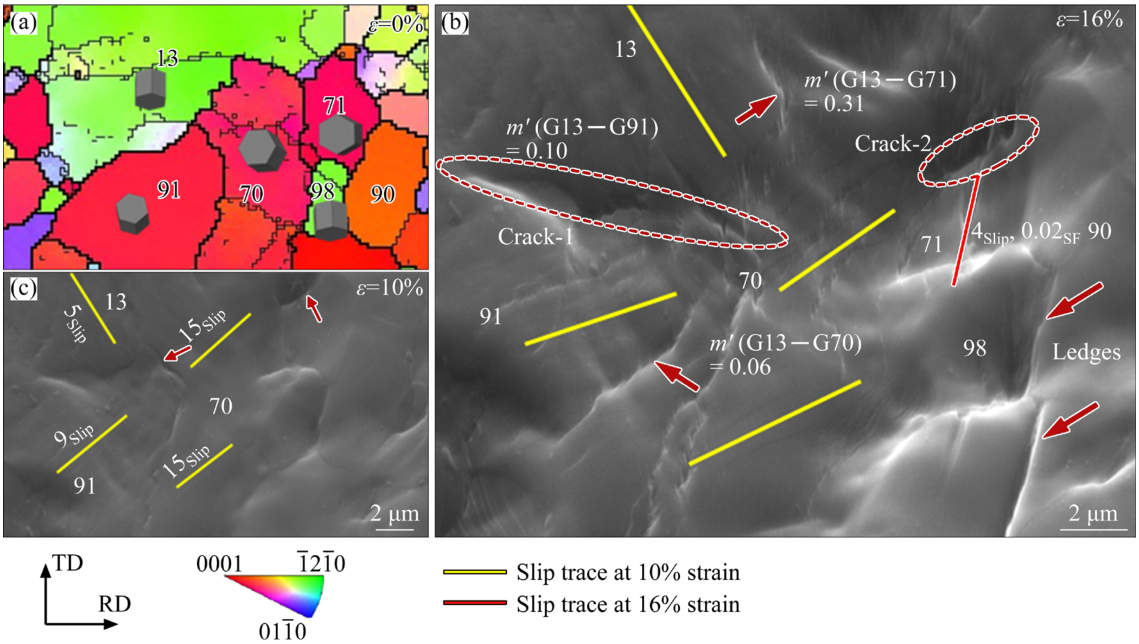

Fig. 9 Fracture behavior between coarse and fine grains in nonuniform microstructure: (a) IPF map; (b, c) SEM images

microstructure before deformation. With the increase of deformation, the ledges gradually manifest at the grain boundary between coarse and fine grains, culminating in intergranular fracture development, as evidenced in Figs. 10(b, c).

In Fig. 10(e), the positions of Cracks A, B, C, and D are marked by yellow dashed lines, and the grain sizes on both sides of the dotted lines are quite different. With the increase of macroscopic strain, dislocations in the small-sized grains steadily accumulate, resulting in lattice distortion, and the stress is gradually concentrated there. When the fine grains cannot continue to adapt to the deformation of the adjacent coarse grains, the initiation of cracks becomes inevitable.

In addition to the difference in the grain size within the grains around Cracks A, B, C, and D, the local strain concentration is also exacerbated by the activation of slip systems within some grains.

Within the microstructure, there are slip traces in G83, G135, and G113. According to the identification of the slip trace, the activated slip systems are the second-order pyramidal $\langle c+a\rangle$ slip $(\bar{1}\bar{1}22)[\bar{1}\bar{1}2\bar{3}]$, prismatic $\langle a\rangle$ slip $(\bar{1}100)[\bar{1}\bar{1}20]$ and basal $\langle a\rangle$ slip $(0001)[2\bar{1}\bar{1}0]$. The ledge is more likely to occur between the grains with slip system activation and the surrounding grains, which is attributable to the nonuniform deformation of magnesium alloy. The grains of the active slip system undergo heightened deformation, consequently fostering stress concentration via dislocation accumulation, manifested as a ledge, such as Crack F. Consequently, the generation of Cracks B and D is not only due to the easier generation of ledges between coarse and fine grains but also related to the fact that the G135 and G113 activated slip systems are more likely to cause dislocation accumulation. The emergence of Crack E is similarly influenced by the propagation of Cracks B and C around it, except that it is affected by the active slip system in G113. Finally, two crack bands (yellow dashed line) formed by Cracks A−F propagation are observed at tensile fracture (Fig. 10(d)).

The mechanism of cracks between coarse and fine grains within the uniform and nonuniform microstructure of the magnesium alloy, as delineated above, is elucidated in Fig. 11. The yellow line indicates the slip trace, and the larger the yellow area, the denser the slip trace in grain, and the more the number of activated slip systems. During the initial phase of deformation (Stage I), a large number of slip systems become activated in the coarse grains, and the generation of coarse strains needs to be coordinated by the surrounding grains. With the increase of the strain (Stage II), the large strain in the coarse grains cannot be completely coordinated by the surrounding fine grains, resulting in the accumulation of dislocations

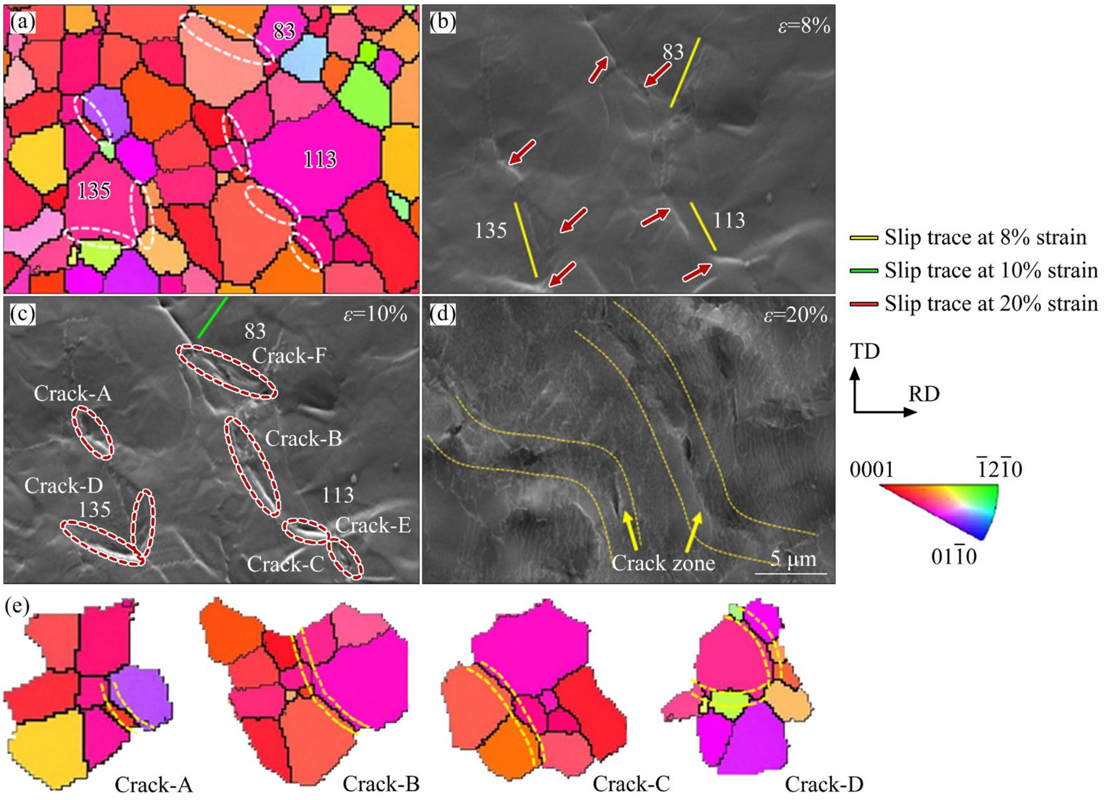

Fig. 10 Fracture behavior between coarse and fine grains in uniform microstructure: (a) IPF map; (b, c, d) SEM images; (e) Cracked area

at the grain boundaries. Moreover, the strain incompatibility between the coarse and fine grains aggravates the strain transmission obstruction between the grains. When the deformation reaches Stage III, the strain that can be coordinated by the fine grains reaches its upper limit. The strain in coarse grains results in the continuous accumulation of dislocations at grain boundaries, the development of the ledge at the common boundaries, and ultimately, the evolution into cracks.

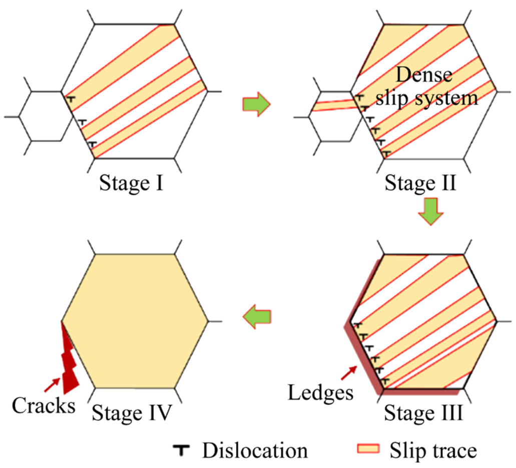

Fig. 11 Mechanism of cracks between coarse and fine grains in nonuniform microstructure

4.3 Fracture behavior affected by LAGB

During annealing, recrystallization and grain growth generally occur [31,32], so the annealing temperature should not be too high, and the annealing time should not be too long to prevent excessive grain growth, which may affect the grain refinement effect [33]. However, the different sizes of grains in the nonuniform microstructure have different requirements for annealing conditions [34]. Dense shear band is depended on the higher stress preferential recrystallization to form fine grains. In contrast, the annealing time required for recrystallization of coarse grains in sparse shear bands is longer, which leads to excessive growth of grains formed by recrystallization of dense shear bands and affects the overall grain refinement effect [35]. Therefore, the nonuniform microstructure has many grains that are not fully annealed, and LAGB is extremely easy to be found internally.

Figure 12 depicts the deformation behavior influenced by LAGB in the nonuniform microstructure of AZ31 Mg alloys. In Fig. 12(a), numerous LAGBs are inside the original annealed microstructure. During the uniaxial tensile loading, different parts of coarse grains experience varying local stresses, generating various slip systems to coordinate plastic deformation (Fig. 12(a_2)). With increasing strain and slip activation, more dislocations accumulate along LAGBs, eventually forming new ledges at LAGB (Fig. 12(a_3)). Therefore, in addition to the generation of the ledge along the high-angle grain boundaries (HAGBs) within the coarse grains, the ledge is also formed along the LAGBs, which can be used as potential positions for crack initiation.

Figure 12(b) illustrates a grain that is about to be fully recrystallized with an LAGB extending through the grain. the kernel average misorientation (KAM) distribution shows high-value KAM concentrated at the LAGB, and the KAM value is proportional to the dislocation density [36], indicating more dislocations accumulation at the LAGB. The analysis in Fig. 6 above shows that the crack formation at the common grain boundaries of Grains G29 and G42 results from local strain incoordination. With deeper and more pronounced slip traces near LAGBs in G42 compared to G29, a high density of slip is more likely to activate near the LAGB. Such grains that are about to fully recrystallize are extremely common in the annealed microstructure, prone to ledge formation at grain boundaries of smaller-sized sub-grains (Figs. 12(b, c)). Moreover, when slip is activated in all grains adjacent to such sub-grains, as shown in Fig. 12(c_2), a large number of slip systems are activated within G55, G56, G64, G73, and G80, and m' values between different deformation systems within the grain pairs G55−G73, G56−G80, and G80−G73 are 0.45, 0.16, and 0.08, respectively. This shows that the strain incompatibility between the grains around the subgrain forces the subgrain to coordinate more deformation and kinking occurs, which causes stress concentration and thus leads to the transgranular fracture.

The deformation mechanism of nonuniform microstructure affected by LAGB is shown in Fig. 13. When a large amount of LAGB is present in the initial grain, different local strains in different parts of the grain activate multiple slip systems

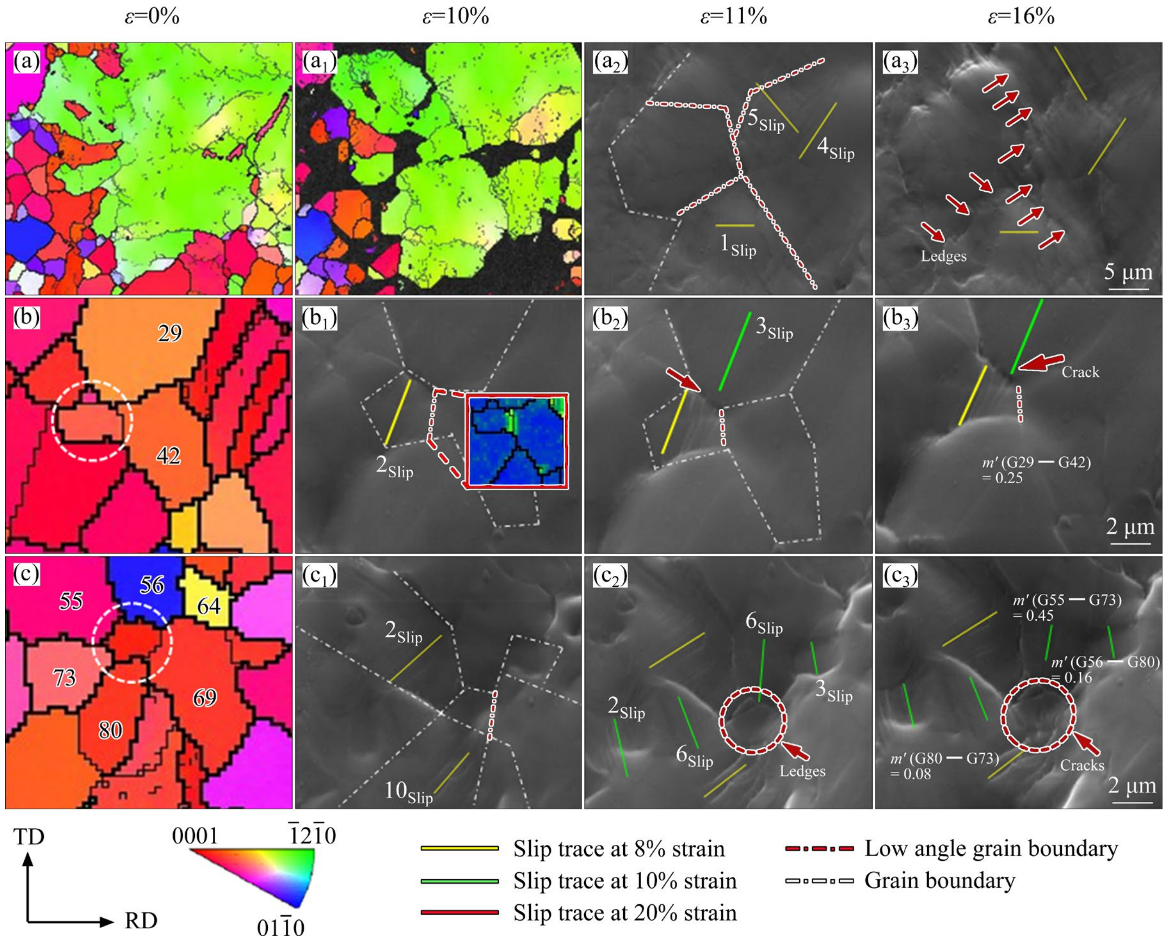

Fig. 12 Deformation behavior affected by LAGB: (a, a_1, b, c) IPF maps; (a_2, a_3, b_{1-3}, c_{1-3}) SEM images at different strain stages

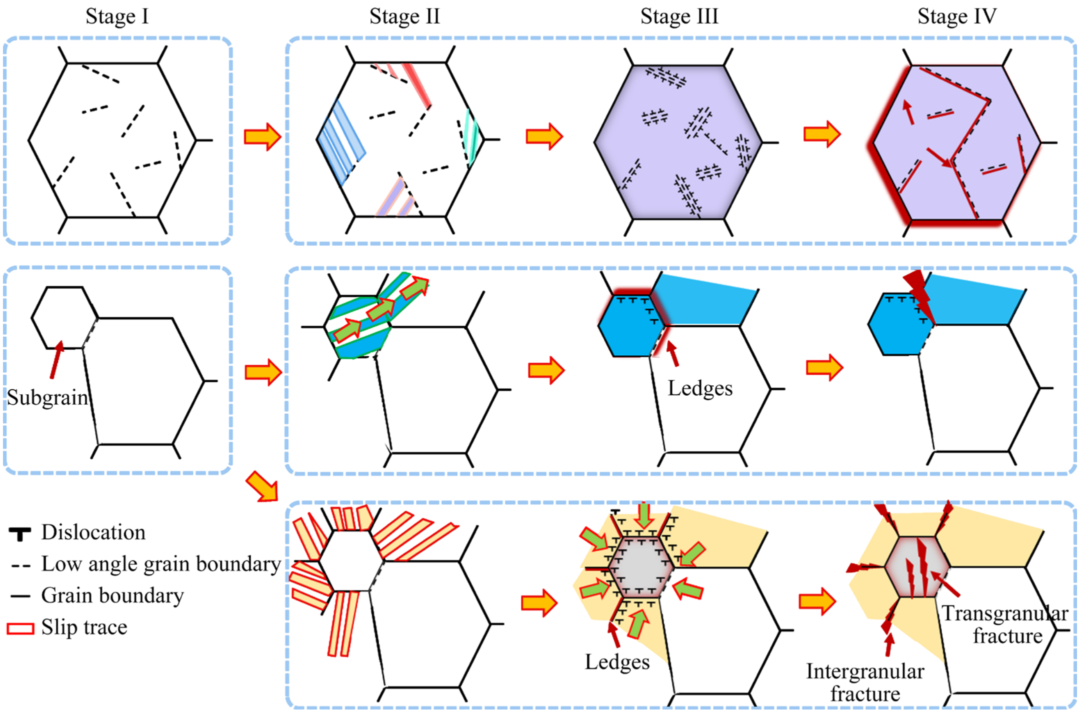

Fig. 13 Deformation mechanism of nonuniform microstructure affected by LAGB

during loading (Stage II). When the slip encounters the LAGB, it forces the dislocation motion to be blocked and pile up near the LAGB, causing strain concentration, eventually, forming ledges (Stage III). There are only a few LAGBs in the grains that are about to be fully recrystallized. If slip is generated in the grain, the high-density slip system tends to be activated around the LAGB. Incompatibility between adjacent grains hinders slip transfer, causing dislocation accumulation and ledge formation at common grain boundaries, leading to crack initiation. If there is no slip in the sub-grain and the surrounding grains all produce a slip system, the sub-grain as the central grain cannot coordinate the deformation of the surrounding grains, and a large number of dislocations accumulate around the sub-grain and the common grain boundary, forcing the sub-grain to kink deformation, and the ledges are formed at common grain boundary (Stage III). Eventually, cracks are formed at the common grain boundary, and the subgrain is affected by the surrounding grains and undergoes transgranular fracture.

5 Conclusions

(1) Multi-pass restricted rolling significantly reduces shear bands in magnesium alloys, increases recrystallization, and enhances microstructure uniformity.

(2) Nonuniform deformation can lead to local strain incompatibility, resulting in strain asynchrony between adjacent grains or adjacent grain pairs, and subsequent relative misalignment occurs, which can gradually develop into cracks. The presence of a nonuniform microstructure exacerbates the occurrence of this fracture mechanism.

(3) Large strains within coarse grains cannot be fully coordinated by surrounding fine grains, resulting in dislocation accumulation at grain boundaries. As the strain that can be coordinated by the fine grains reaches its upper limit, the common grain boundaries gradually produce ledges that can propagate into cracks.

(4) Low-angle grain boundaries can also affect the fracture behavior of Mg alloys. LAGB in coarse grains accumulate dislocations along the LAGB to form ledges, while fine grains penetrated by LAGB are prone to becoming strain concentration, leading to intergranular fracture and transgranular fracture.

CRediT authorship contribution statement

Jing TIAN: Conceptualization, Methodology, Investigation, Formal analysis, Writing – Original draft, Writing – Review & editing; **Jia-fei DENG:** Conceptualization, Formal analysis, Investigation; **Wei**

LIANG: Funding acquisition, Resources, Supervision; **Xi ZHAO:** Formal analysis, Resources; **Xiao-gang WANG:** Resources.

Declaration of competing interest

The authors declare that they have no known competing financial interests or personal relationships that could have appeared to influence the work reported in this paper.

Acknowledgments

This study was supported by the National Natural Science Foundation of China (No. U1810208), and Shanxi Province Science and Technology Major Projects, China (No. 2018110100).

References

[1] SONG Jiang-feng, CHEN Jing, XIONG Xiao-ming, PENG Xiao-dong, CHEN Dao-lun, PAN Fu-sheng. Research advances of magnesium and magnesium alloys worldwide in 2021 [J]. Journal of Magnesium and Alloys, 2022, 10(4): 863−898.

[2] YANG Yan, XIONG Xiao-ming, CHEN Jing, PENG Xiao-dong, CHEN Dao-lun, PAN Fu-sheng. Research advances in magnesium and magnesium alloys worldwide in 2020 [J]. Journal of Magnesium and Alloys, 2021, 9(3): 705−747.

[3] PRASAD S V S, PRASAD S B, VERMA K, MISHRA R K, KUMAR V, SINGH S. The role and significance of Magnesium in modern day research—A review [J]. Journal of Magnesium and Alloys, 2022, 10(1): 1−61.

[4] BETTLES C, BARNETT M. Advances in wrought magnesium alloys [M]. Woodhead Publishing Limited, 2012.

[5] YI S B, DAVIES C H J, BROKMEIER H G, BOLMARO R E, KAINER K U, HOMEYER J. Deformation and texture evolution in AZ31 magnesium alloy during uniaxial loading [J]. Acta Materialia, 2006, 54: 549−562.

[6] AYDıNER C C, TELEMEZ M A. Multiscale deformation heterogeneity in twinning magnesium investigated with in situ image correlation [J]. International Journal of Plasticity, 2014, 56: 203−218.

[7] MARTIN G, SINCLAIR C W, SCHMITT J H. Plastic strain heterogeneities in an Mg−1Zn−0.5Nd alloy [J]. Scripta Materialia, 2013, 68: 695−698.

[8] TIAN Jing, LU Hui-hu, ZHANG Wang-gang, NIE Hui-hui, SHI Quan-xin, DENG Jia-fei, WANG Li-fei. An effective rolling process of magnesium alloys for suppressing edge cracks: Width-limited rolling [J]. Journal of Magnesium and Alloys, 2022, 10(8): 2193−2207.

[9] HUO Peng-da, LI Feng, WANG Ye, WU Rui-zhi, GAO Rong-he, ZHANG An-xin. Annealing coordinates the deformation of shear band to improve the microstructure difference and simultaneously promote the strength−plasticity of composite plate [J]. Materials & Design, 2022, 219: 110696.

[10] TIAN Jing, DENG Jia-fei, CHANG Yuan-ying, SHI Quan-xin, LIANG Wei, MA Jin-yao. A study of unstable fracture of a magnesium alloy caused by uneven microstructure [J]. Materials Letters, 2022, 314: 131799.

[11] ZHA Min, ZHANG Hong-min, JIA Hai-long, GAO Yi-peng, JIN Shen-bao, SHA Gang, LI Yan-jun. Prominent role of multi-scale microstructural heterogeneities on superplastic deformation of a high solid solution Al−7Mg alloy [J]. International Journal of Plasticity, 2021, 146: 103108.

[12] DENG Jia-fei, TIAN Jing, ZHOU Yan-cai, CHANG Yuan-ying, LIANG Wei, MA Jin-yao. Quasi-in-situ analysis of as-rolled microstructure of magnesium alloys during annealing and subsequent plastic deformation [J]. Materials, 2022, 15(19): 6581.

[13] SUN D K, CHANG C P. Microstructural study of strain localization in a compressed Mg−3Al−1Zn alloy [J]. Materials Science and Engineering A, 2014, 603: 30−36.

[14] SCOTT J, MILES M, FULLWOOD D, ADAMS B, KHOSRAVANI A, MISHRA R K. Room temperature shear band development in highly twinned wrought magnesium AZ31B sheet [J]. Metallurgical and Materials Transactions A, 2012, 44: 512−516.

[15] MWEMBELA A, KONOPLEVA E B, MCQUEEN H J. Microstructural development in Mg alloy AZ31 during hot working [J]. Scripta Materialia, 1997, 37(11): 1789−1795.

[16] YI S, SCHESTAKOW I, ZAEFFERER S. Twinning-related microstructural evolution during hot rolling and subsequent annealing of pure magnesium [J]. Materials Science and Engineering A, 2009, 516: 58−64.

[17] BARNETT M R, NAVE M D, GHADERI A. Yield point elongation due to twinning in a magnesium alloy [J]. Acta Materialia, 2012, 60: 1433−1443.

[18] DUDAMELL N V, ULACIA I, GÁLVEZ F, YI S, BOHLEN J, LETZIG D, PÉREZ-PRADO M T. Twinning and grain subdivision during dynamic deformation of a Mg AZ31 sheet alloy at room temperature [J]. Acta Materialia, 2011, 59: 6949−6962.

[19] CHEN Wei, XIAO Lin, SUN Qiao-yan, SUN Jun. Effect of the initial grain size on grain refinement in Ti−2Al−2.5Zr alloy subjected to multi-impact process [J]. Materials Science and Engineering A, 2012, 554: 86−94.

[20] CHRISTIAN J W, MAHAJAN S. Deformation twinning [J]. Progress in Materials Science, 1995, 39(1): 1−157.

[21] YIN D D, BOEHLERT C J, LONG L J, HUANG G H, ZHOU H, ZHENG J, WANG Q D. Tension−compression asymmetry and the underlying slip/twinning activity in extruded Mg−Y sheets [J]. International Journal of Plasticity, 2021, 136: 102878.

[22] ZHU Gao-ming, WANG Le-yun, ZHOU Hao, WANG Jin-hui, SHEN Yao, TU Peng, ZENG Xiao-qin. Improving ductility of a Mg alloy via non-basal $\langle a \rangle$ slip induced by Ca addition [J]. International Journal of Plasticity, 2019, 120: 164−179.

[23] DENG Jia-fei, TIAN Jing, CHANG Yuan-ying, ZHOU Yan-cai, LIANG Wei, MA Jin-yao. The role of $\{10\bar{1}2\}$ tensile twinning in plastic deformation and fracture prevention of magnesium alloys [J]. Materials Science and Engineering A, 2022, 853: 143678.

[24] DENG Jia-fei, TIAN Jing, ZHOU Yan-cai, CHANG Yuan-ying, LIANG Wei, MA Jin-yao. Plastic deformation

mechanism and hardening mechanism of rolled rare-earth magnesium alloy thin sheet [J]. Materials & Design, 2022, 218: 110678.

[25] DENG Jia-fei, TIAN Jing, ZHOU Yan-cai, CHANG Yuan-ying, LIANG Wei, MA Jin-yao. Plastic deformation and fracture mechanisms of rolled Mg−8Gd−4Y−Zn and AZ31 magnesium alloys [J]. Materials & Design, 2022, 223: 111179.

[26] LUNT D, THOMAS R, ATKINSON M D, SMITH A, SANDALA R, FONSECA J Q, PREUSS M. Understanding the role of local texture variation on slip activity in a two-phase titanium alloy [J]. Acta Materialia, 2021, 216: 117111.

[27] BOEHLERT C J, CHEN Z, GUTIÉRREZ-URRUTIA I, LLORCA J, PÉREZ-PRADO M T. In situ analysis of the tensile and tensile-creep deformation mechanisms in rolled AZ31 [J]. Acta Materialia, 2012, 60: 1889−1904.

[28] NI R, MA S J, LONG L J, ZHENG J, ZHOU H, WANG Q D, YIN D D. Effects of precipitate on the slip activity and plastic heterogeneity of Mg−11Y−5Gd−2Zn−0.5Zr (wt.%) during room temperature compression [J]. Materials Science and Engineering A, 2021, 804: 140738.

[29] ZHOU Bi-jin, WANG Le-yun, JIN Pei-peng, JIA Hai-long, ROVEN H J, ZENG Xiao-qin, LI Yan-jun. Revealing slip-induced extension twinning behaviors dominated by micro deformation in a magnesium alloy [J]. International Journal of Plasticity, 2020, 128: 102669.

[30] WANG F, SANDLÖBES S, DIEHL M, SHARMA L, ROTERS F, RAABE D. In situ observation of collective grain-scale mechanics in Mg and Mg–rare earth alloys [J]. Acta Materialia, 2014, 80: 77−93.

[31] BURKE J E, TURNBULL D. Recrystallization and grain growth [J]. Progress in Metal Physics, 1952, 3: 220−292.

[32] HAN Fang, LUO Xuan, MARTHINSEN K, WU Gui-lin, HOU Zi-yong, HUANG Xiao-xu. Effect of initial grain size on the recrystallization behavior and recrystallization texture of a Mg−3Gd alloy [J]. Journal of Materials Science & Technology, 2024, 188: 169−182.

[33] JIANG Wen-ting, REN Xin-yu, YU Lei, SUN Jing-li, NI Song, HUANG Yi, SONG Min. Twinning-assisted static recrystallization and texture evolution in a Mg−Gd−Y−Zr alloy [J]. Journal of Materials Research and Technology, 2024, 28: 4250−4261.

[34] LOPEZ-SANCHEZ M A, TOMMASI A, BAROU F, QUEY R. Dislocation-driven recrystallization in AZ31B magnesium alloy imaged by quasi-in situ EBSD in annealing experiments [J]. Materials Characterization, 2020, 165: 110382.

[35] TIAN Jing, DENG Jia-fei, MA Rong, CHANG Yuan-yin, LIANG Wei, MA Jin-yao. Pre-control of annealing temperature on the uniformity of deformed structure of wrought magnesium alloy [J]. Materials Letters, 2021, 305: 130820.

[36] GUGLIELMI P O, ZIEHMER M, LILLEODDEN E T. On a novel strain indicator based on uncorrelated misorientation angles for correlating dislocation density to local strength [J]. Acta Materialia, 2018, 150: 195−205.

基于滑移迹线分析的镁合金轧板组织均匀性对断裂行为的影响

田 静[1,2,3,4]，邓嘉飞[2,3,4]，梁 伟[2,3,4]，赵 熹[1]，王小刚[5]

1. 中北大学 航空宇航学院，太原 030051；
2. 太原理工大学 分析测试中心，太原 030024；
3. 太原理工大学 材料科学与工程学院，太原 030024；
4. 太原理工大学 先进镁基材料山西省重点实验室，太原 030024；
5. 山西银光华盛镁业股份有限公司，闻喜 043800

摘 要：镁合金轧板组织的不均匀性往往影响其塑性变形能力。采用多道次限制轧制的方法成功制备了组织均匀的 AZ31 镁合金轧板，提高了板材的力学性能。采用准原位拉伸 EBSD 方法研究了组织均匀性对镁合金塑性变形和断裂行为的影响。结果表明，镁合金组织的不均匀性会加剧相邻晶粒之间的应变异步性，产生相对错位并发展为裂纹。细晶不足以协调其相邻粗晶粒内的应变，导致粗晶粒在其共同晶界处产生晶阶。此外，低角度晶界也会影响断裂行为，低角度晶界穿透的小晶粒更容易成为引起晶间断裂的应变集中区，甚至导致穿晶断裂。

关键词：AZ31 镁合金；轧制；显微组织；断裂行为；塑性变形

(Edited by Bing YANG)